Experimental study of particle transport and density fluctuations in LHD

INSTITUTE OF PHYSICS PUBLISHING and INTERNATIONAL ATOMIC ENERGY AGENCY NUCLEAR FUSION

Nucl. Fusion **46** (2006) 110–122 doi:10.1088/0029-5515/46/1/013

Experimental study of particle transport and density fluctuations in LHD

K. Tanaka[1], C. Michael[1], A.L. Sanin[2], L.N. Vyacheslavov[2], K. Kawahata[1], S. Murakami[3], A. Wakasa[4] , S. Okajima[5], H. Yamada[1], M. Shoji[1], J. Miyazawa[1], S. Morita[1], T. Tokuzawa[1], T. Akiyama[1], M. Goto[1], K. Ida[1], M. Yoshinuma[1], I. Yamada[1], M. Yokoyama[1], S. Masuzaki[1], T. Morisaki[1], R. Sakamoto[1], H. Funaba[1], S. Inagaki[1], M. Kobayashi[1], A. Komori[1] and LHD experimental group

[1] National Institute for Fusion Science, 322-6 Oroshi, Toki, 509-5292, Japan
[2] Budker Institute of Nuclear Physics, 630090, Novosibirsk, Russia
[3] Department of Nuclear Engineering, Kyoto University, Kyoto 606-8501, Japan
[4] Graduate School of Engineering, Hokkaido University, Sapporo, 060-8628, Japan
[5] Department of Engineering, Chubu Univertsity, Kasugai, 487-8501, Japan

E-mail: ktanaka@LHD.nifs.ac.jp

Received 11 December 2004, accepted for publication 11 November 2005
Published 22 December 2005
Online at stacks.iop.org/NF/46/110

Abstract

A variety of electron density (n_e) profiles have been observed in the Large Helical Device (LHD). The density profiles change dramatically with heating power and toroidal magnetic field (B_t). The particle transport coefficients, i.e. diffusion coefficient (D) and convection velocity (V) are experimentally obtained in the standard configuration from density modulation experiments. The values of D and V are estimated separately in the core and edge. The diffusion coefficients are found to be a function of electron temperature (T_e), and vary with B_t. Edge diffusion coefficients are proportional to $B_t^{-0.73\pm0.23}$. Non-zero V is observed, and it is found that the electron temperature gradient can drive particle convection, particularly in the core region. The convection velocity both in the core and edge reverses direction from inward to outward as the T_e gradient increases. However, the toroidal magnetic field also significantly affects the value and direction of V. The density fluctuation profiles are measured by a two-dimensional phase contrast interferometer. It was found that fluctuations which are localized in the edge propagate towards the ion diamagnetic direction in the laboratory frame, while the phase velocity of fluctuations around mid-radius is close to the plasma poloidal $E_r \times B_t$ rotation velocity. The fluctuation level becomes larger as particle flux becomes larger in the edge region.

PACS numbers: 52.55.Hc, 52.25.Fi, 52.35.Ra

(Some figures in this article are in colour only in the electronic version)

1. Introduction

Particle transport of bulk ions and electrons is one of the most important issues in magnetically confined plasma research. However, compared with energy transport study, fewer works have been done. This is because of the difficulties of the experimental estimation of the particle source and the existence of the convection term in the particle balance equation. These make the estimation of particle transport coefficients, i.e. diffusion coefficients (D) and convection velocity (V), impossible from simple particle balance analysis in the equilibrium state. Large Helical Device (LHD) is a large heliotron whose operational envelope extends towards the fusion relevant regime. Although thermal transport has been discussed in many reports, this is the first systematic study of the bulk ion and electron particle transport in LHD. The diffusion coefficients and convection velocities are separately estimated from the propagation of periodically modulated density by controlling the gas puff.

In most operational regimes of LHD, particle transport is dominated by anomalous transport. Therefore, the experimental study of turbulence is also important. In this

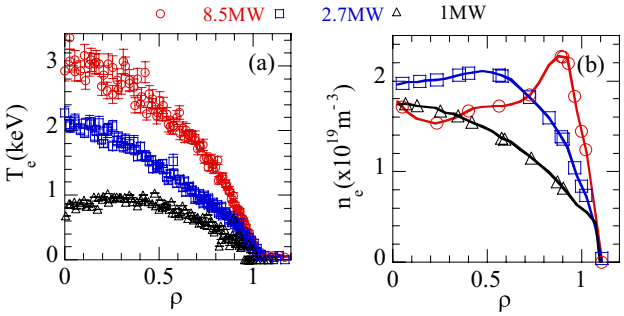

Figure 1. (*a*) Electron temperature and (*b*) density profiles under different NBI heating power. At $R_{ax} = 3.6$ m, $B_t = 2.75$ T for 2.7 MW and 8.5 MW heating, $B_t = 2.8$ T for 1 MW heating. Symbols in (*b*) indicate corresponding chord position of interferometers.

paper, characteristics of electron density fluctuations, which can play a role on particle confinements, are also described.

2. Density profiles in LHD

The density profiles in LHD change with the magnetic configuration, magnetic field strength and heating power. This is because the characteristics of particle transport are determined by these experimental conditions. Figure 1 shows T_e and n_e profiles at different neutral beam injection (NBI) heating power. Temperature profiles are measured by Thomson scattering [1], and density profiles are measured by CO_2 laser pumped CH_3OH 119 μm far infrared (FIR) [2] and CO_2 10.6 μm infrared (IR) [3] laser interferometers. The magnetic configuration is the so-called standard configuration, whose magnetic axis position (R_{ax}) is 3.6 m. This configuration has the largest plasma volume and achieves the highest stored energy and best energy confinement improvement [4].

As shown in figure 1(*a*), T_e increases with increasing heating power. The shape of the T_e profiles remains parabolic and peaked at the centre almost regardless of the heating power. On the other hand, n_e profiles change dramatically from peaked to hollow with increase of the heating power. The value of n_e is non-zero at the last closed flux surface (LCFS), which is labelled as having a normalized radius ρ equal to 1, although T_e is almost zero at this position. This is due to the existence of an ergodic region, which has finite connection length and is located outside of LCFS. The plasma can be confined in this ergodic region. It is known from measurements of the spatial profile of H_α radiation that the peak of the particle source is always located outside of the LCFS surface when n_e at $\rho = 1$ is higher than 1×10^{18} m^{-3} [5]. In addition, particle fuelling from NBI is negligible in these cases. Therefore, the distinction between n_e profiles in figure 1(*b*) is not due to the difference of the particle source deposition but due to the dissimilarity in the transport. The density profiles also vary with magnetic configuration. At similar collision frequencies, the n_e profiles tend to become more hollow as R_{ax} increases [6]. In this paper, we concentrate only on the dependence of particle transport on heating power and B_t in the standard configuration. The heating scheme used is NBI, whose power is scanned from 1 MW to 8.7 MW in this series of experiments.

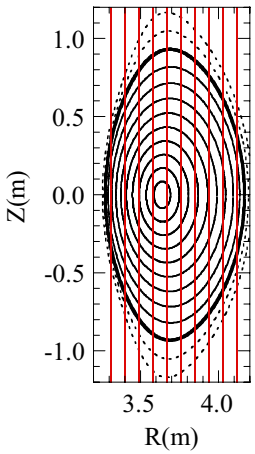

Figure 2. Measured cross section of FIR laser interferometer. Magnetic flux surfaces are shown every $\rho = 0.1$ step from $\rho = 0.1$ to 1.2. Magnetic configuration is standard configuration ($R_{ax} = 3.6$ m, $\beta = 0\%$). The vertical lines mark the path of FIR laser beam used for analysis. Ten of 13 channels, which were used for the analysis are shown.

3. Density modulation experiments in LHD

The data of FIR laser interferometer was used for the analysis of modulation experiments. Figure 2 shows the plasma cross section with chord positions of 13 channels FIR laser interferometer. The FIR interferometer covers the whole region of the plasma with 90 mm spacing. The interferometer is an appropriate diagnostic, because it enables measurement of the modulation cycles with good time resolution and since it employs phase measurements, the results are unaffected by change of the sensitivities of the detector and laser power. However, the measured quantities are line integrated values along the viewing chords. Therefore, mathematical processing should be done for interpretation of the data.

At standard configuration ($R_{ax} = 3.6$ m), the signal is visible from $R = 3.309$ m to $R = 4.209$ m. The outermost chord , which is at $R = 4.209$ m, shows very small line density, although the neighbour channel, which is at $R = 4.119$ m, shows clear signal. In this analysis, $R = 4.2$ m is assumed to be plasma boundary. This plasma boundary is supported by the recent measurements by the CO_2 laser imaging interferometer [3]. For the analysis of phase and amplitude of the density modulation, ten channels, which are located from $R = 3.309$ m to $R = 4.119$ m were used. The ten channels samples are from $\rho = 0.1$ up to around $\rho = 1.0$ with roughly every $\rho = 0.1$ step as shown in figure 2.

3.1. Analysis technique

The particle flux can be written as the sum of diffusion and convection terms as follows:

$$\Gamma = -D\nabla n_e + n_e V. \tag{1}$$

The particle balance equation is the following:

$$\frac{\partial n_e}{\partial t} = -\nabla \cdot \Gamma + S = -\frac{1}{r}\frac{\partial}{\partial r} r\Gamma + S. \tag{2}$$

Here, S is particle source rate. For the modulated part of the density the following equations are obtained in cylindrical geometry.

$$n_e = n_{e\,eq} + \tilde{n}, \qquad \Gamma = \Gamma_{eq} + \tilde{\Gamma}, \qquad S = S_{eq} + \tilde{S}, \tag{3}$$

$$\tilde{S} = \tilde{S}e^{i\omega t}, \qquad \tilde{n}_e = \tilde{n}_e e^{i\omega t}, \qquad \frac{\partial \tilde{n}_e}{\partial t} = i\omega \tilde{n}_e, \tag{4}$$

$$\frac{\partial^2 \tilde{n}_e}{\partial r^2} + \left(\frac{1}{r} + \frac{1}{D}\frac{\partial D}{\partial r} - \frac{V}{D}\right)\frac{\partial \tilde{n}_e}{\partial r} - \left(\frac{V}{rD} + \frac{1}{D}\frac{\partial V}{\partial r}\right)\tilde{n}_e - i\frac{\omega}{D}\tilde{n}_e + \frac{\tilde{S}}{D} = 0. \tag{5}$$

Here, subscript eq, tilde symbols and ω indicate equilibrium values, modulated components and modulation frequency, respectively. Since the particle source is localized in the plasma edge, the modulated particle source induces a density perturbation propagating from the edge to the core. The parameters D and V characterize this propagation. From the analysis of modulated components, D and V can be determined independently of the absolute value of the particle source rate [7], which is difficult to estimate experimentally. The particle source profiles are estimated by a neutral particle transport simulation code DEGAS [8], which can take into account the complicated three-dimensional shape of the LHD plasma and the vacuum vessel [9].

The neutral penetration speed is of the order of a kilometre per second, while the penetration speed of density modulation is of the order of a metre per second. Therefore, the shape of the modulated particle source rate is assumed to be equal to that of the equilibrium one, and spatial phase variation of the modulated source is neglected.

In equation (5), $\tilde{n}_e$ is a complex function ($\tilde{n}_e = \tilde{n}_{eR} + i\tilde{n}_{eI}$), and it consists of real and imaginary parts. Then, the real part of equation (5) can be written in the following form:

$$\frac{\partial^2 \tilde{n}_{eR}}{\partial r^2} + \left(\frac{1}{r} + \frac{1}{D}\frac{\partial D}{\partial r} - \frac{V}{D}\right)\frac{\partial \tilde{n}_{eR}}{\partial r} - \left(\frac{V}{rD} + \frac{1}{D}\frac{\partial V}{\partial r}\right)\tilde{n}_{eR} + \frac{\omega}{D}\tilde{n}_{eI} + \frac{\tilde{S}}{D} = 0, \tag{6}$$

and the imaginary part can be written as

$$\frac{\partial^2 \tilde{n}_{eI}}{\partial r^2} + \left(\frac{1}{r} + \frac{1}{D}\frac{\partial D}{\partial r} - \frac{V}{D}\right)\frac{\partial \tilde{n}_{eI}}{\partial r} - \left(\frac{V}{rD} + \frac{1}{D}\frac{\partial V}{\partial r}\right)\tilde{n}_{eI} - \frac{\omega}{D}\tilde{n}_{eR} = 0, \tag{7}$$

where $\tilde{n}_{eR}$ and $\tilde{n}_{eI}$ are functions of the magnetic flux surface. Equations (6) and (7) are solved numerically by using the matrix technique [10, 11] with the following boundary condition.

$$\frac{\partial \tilde{n}_{eR}}{\partial r} = \frac{\partial \tilde{n}_{eI}}{\partial r} = 0 \text{ at } r = 0, \qquad \tilde{n}_{eR} = \tilde{n}_{eI} = 0 \text{ at } r = a_{BC}$$

a_{BC} is average radius of the plasma boundary. (8)

The value of D and V can be determined from the numerical optimized fitting to minimize the following χ^2 value:

$$\chi^2_{mod\_radial} = \int ((\tilde{n}_{eR\_exp} - \tilde{n}_{eR\_calc})^2 + (\tilde{n}_{eI\_exp} - \tilde{n}_{eI\_calc})^2)\,dr. \tag{9}$$

In equation (9), the subscripts 'exp' and 'calc' indicate experimentally observed values and calculated values from equation (6) and (7) with supposed $D(\rho)$, $V(\rho)$ (see the next section for details) and simulated $\tilde{S}(\rho)$, respectively. The spatial profiles of $\tilde{n}_{eR}$ and $\tilde{n}_{eI}$ are localized in the edge region. With the use of the presently available ten channels of the FIR interferometer, reconstruction of $\tilde{n}_{eR}$ and $\tilde{n}_{eI}$ is not easy especially at high frequency modulation. In this case, the reconstructed radial profile of modulations suffers from contamination of reconstruction errors; therefore, in this paper, we fit the integrated value of $\tilde{n}_{eR\_calc}$ and $\tilde{n}_{eI\_calc}$ along the viewing chord of the interferometer, and the following χ^2 was used for fitting:

$$\chi^2_{mod\_int} = \sum_{ch}\left(\left(\int \tilde{n}_{eR\_exp}\,dl - \int \tilde{n}_{eR\_calc}\,dl\right)^2 + \left(\int \tilde{n}_{eI\_exp}\,dl - \int \tilde{n}_{eI\_calc}\,dl\right)^2\right). \tag{10}$$

In equation (10), $\sum_{ch}$ is a summation of each interferometer chord position's value, and $\int dl$ is the integration along the viewing chord. In addition, the following χ^2 values are minimized simultaneously:

$$\chi^2_{eq} = \int (n_{eq\_exp} - \alpha \cdot n_{eq\_calc})^2\,dr. \tag{11}$$

In equation (11), n_{eq_exp} is the equilibrium density profile, which is obtained from density reconstruction, and n_{eq_calc} is the calculated density profile with the model of $D(\rho)$, $V(\rho)$ and simulated $S(\rho)$, respectively. As described above the shape of $S(\rho)$ is the same as $\tilde{S}(\rho)$. The DEGAS simulation result does not give the absolute value of $S(\rho)$. Therefore, the absolute value of n_{eq_calc}, which is calculated from equation (2) with the condition $\partial n_e/\partial t = 0$ for the equilibrium state, cannot be determined. Then the additional fitting parameter α is used to match n_{eq_exp} and n_{eq_calc}.

Finally the least square fitting is done to minimize the following χ^2:

$$\chi^2_{total} = \chi^2_{mod\_int} + \text{weight} \cdot \chi^2_{eq}. \tag{12}$$

The simultaneous minimizing makes fitting more stable. At high modulation frequency, the modulation amplitude is strongly localized in the edge region. In this case, fitting of the $\chi^2_{mod\_int}$ becomes unstable. The parameter weight is tuned to minimize $\chi^2_{mod\_int}$ and χ^2_{eq} effectively. The parameter weight was 1.0 for 2 Hz , 0.1 for 5 Hz and 0.01 for 10 Hz modulation. The lower weight of the equilibrium fitting at higher modulation frequency is due to the smaller sensitivities of the fitting of modulation components at higher modulation frequency.

There is a discussion on the discrepancy between the transport coefficient of the equilibrium state and that from the transient analysis [12]. For the energy transport analysis, the difference between thermal diffusion coefficients obtained from the power balance analysis and the coefficients from the transient analysis is not negligible for tokamaks. These differences appear due to the existence of the off-diagonal term and the non-linearity of the heat flux to temperature gradient. Recently, a comparison of the transient and equilibrium

thermal diffusion coefficients was made in LHD, and a quantitative difference between power balance and transient analysis was found [13].

For the particle transport analysis, as shown in equation (1), the existence of the off diagonal term is assumed *a priori*. However, the non-linearity of the particle flux can affect the particle transport coefficients obtained from transient analysis [14]. More detailed quantitative consideration will be done in the next section.

3.2. Example of analysis

3.2.1. Example of waveform. Figure 3(*a*) shows a typical wave form of the modulated density. In order to modulate under constant background density, density feedback control was done. Given the reference signals, the applied voltage to gas control valve was automatically adjusted to modulate under constant background density. Without feedback, the background density gradually increases. As shown in figure 3(*d*), the gas puff fuelling rate varies in time. Total particle fuelling, which includes both fuelling from gas puffing and recycling, should be controlled. Therefore, the gas puff fuelling rate was reduced in order to compensate the increase of the background density due to the recycled fuelling as shown in figure 3(*d*). The resultant density and particle fuelling were sinosoidally modulated under approximately constant background between $t = 1.4$ and 2.9 s as shown in figures 3(*a*) and (*c*), respectively. The central averaged density was controlled to within ±3%. The diamagnetic stored energy was controlled to within ±5% indicating the averaged temperature was controlled to within ±2%.

The integrated modulation amplitude and phase are calculated by the correlation analysis after subtracting background averaged density. Figure 4 shows the amplitude spectrum of modulated density components of figure 3(*a*). As shown in figure 4, the harmonic components are less than 10% of the fundamental 5 Hz components so that they should not cause significant non-linear effect. The error was determined as a standard deviation within the frequency resolution (Δf), which is determined by the data length of modulation analysis. The frequency width for the amplitude and phase determination is shown by two arrows in figure 4. Only the normalized amplitude is required for the analysis, because only the shape of the source rate in equation (5) is used for the analysis.

3.2.2. Example of coefficients determination. In this section, determinations of the transport coefficient are described for the different heating power of two discharges; one 5.2 MW NBI heating with 5 Hz modulation and the other 1 MW heating with 2 Hz modulation. The temperature and density profiles are shown in figure 5. Figure 6 shows the integrated amplitude and phase profile of both cases. A clear difference was observed in the two heating cases. Lower modulation frequency allows a deep enough penetration of the perturbation under conditions of lower transport at lower heating power.

The integrated amplitude is normalized by the reference channel signal of correlation analysis, which is chord at $R = 3.669$ m. Figure 6 shows the radial profile of amplitude and phase, which are calculated with the slice and stuck

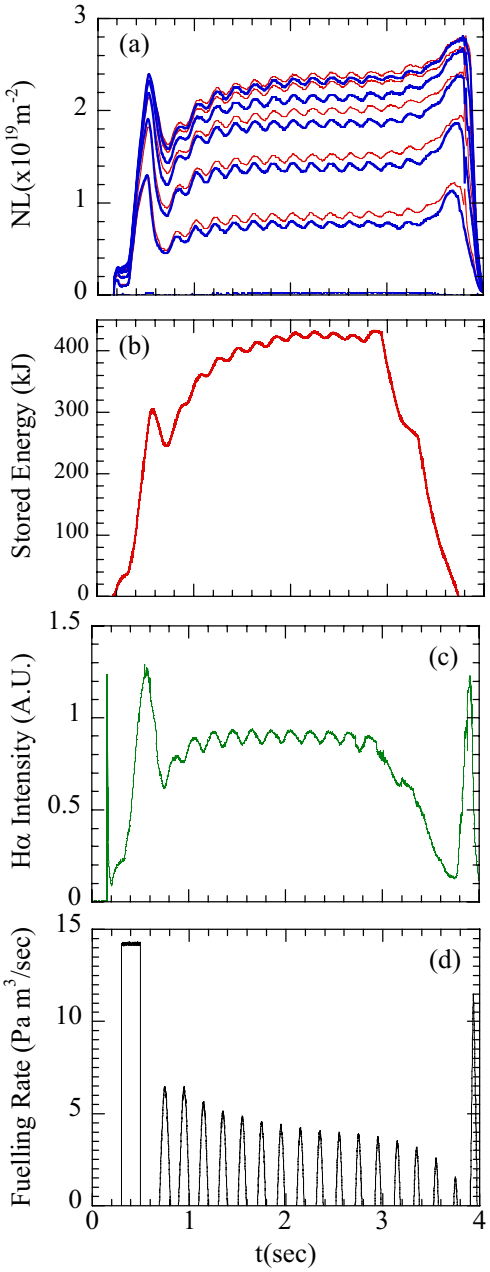

Figure 3. (*a*) Example of modulated density at 5 Hz. Thin red lines indicate modulation at $R = 3.309$, 3.399, 3.489, 3.579, 3.669 m from bottom of the picture. Thick blue lines correspond to modulation at $R = 3.759$, 3.849, 3.939, 4.029, 4.119, 4.209 m from top of the picture. (*b*) diamagnetic stored energy, (*c*) H_α signal intensity and (*d*) gas puff fuelling rate.

density reconstruction [15]. The appropriate flux surface mapping for the reconstruction was determined from the data set of VMEC equilibrium calculation [16] to match the T_e profile on the outer and inner side of the magnetic axis. The reconstructions of the real and imaginary part of integrated modulation are done separately, and then radial amplitude and phase profiles are calculated. In order to determine the reconstruction error, the reconstruction was done 100 times with random error. The standard deviation of the random errors for the reconstruction was taken equal to experimental values

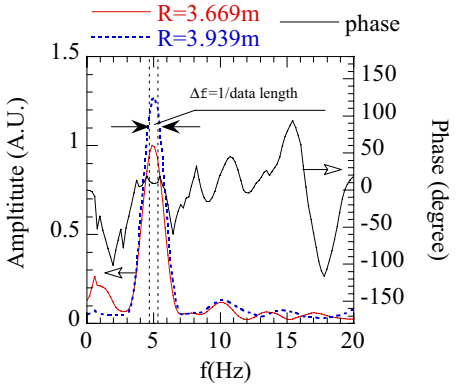

Figure 4. Spectrum of modulated components of electron density.

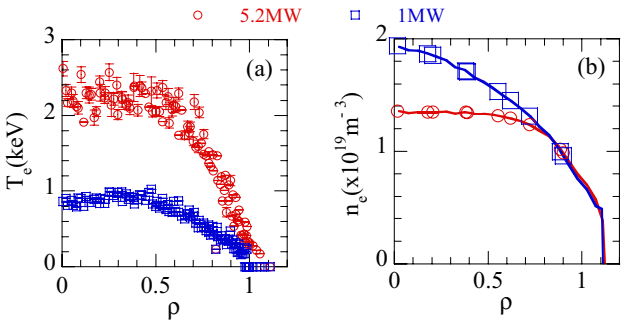

Figure 5. Temperature and density profile of 5.2 and 1 MW NBI heating $R_{ax} = 3.6\,\mathrm{m}$, $B_t = 2.8\,\mathrm{T}$.

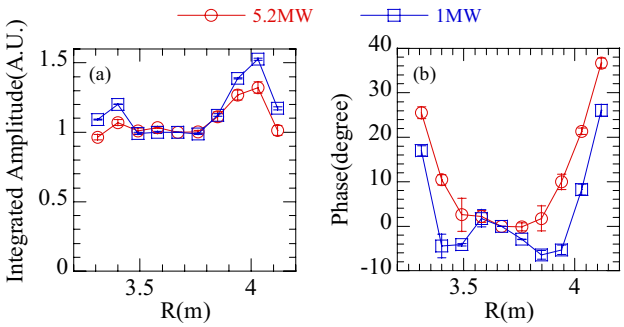

Figure 6. Integrated modulation amplitude and phase profile. Symbols indicate chord positions of the interferometer. A 5 Hz modulation for 5.2 MW and 2 Hz modulation for 1 MW injection were done.

determined from correlation analysis. As shown in figure 7, modulation amplitude is localized in edge in both cases.

Figure 8 shows particle source rate profile calculated from the DEGAS simulation code with the observed T_e and n_e profile. The shapes of the source rate profiles are almost identical.

Ten channels are used for the fitting. For the $\chi^2_{\mathrm{mod\_int}}$ fitting, twenty channels, where ten is for the real part and another ten is for the imaginary part of the fitting, can be used. For the χ^2_{total} fitting an additional ten channels can be used for the equilibrium profile fitting; then, totally, 30 channels are available. However, as shown in figure 7, the modulation amplitude is localized in the edge region; therefore, measured values by interferometer at around the plasma centre do not

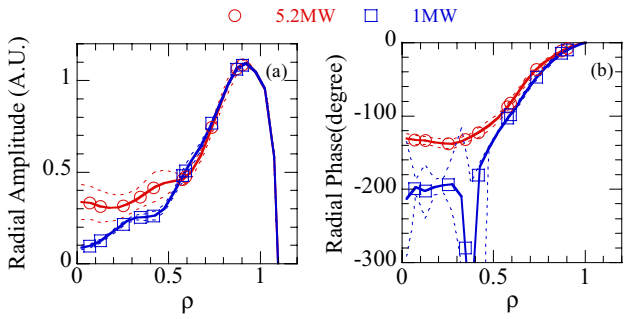

Figure 7. Radial profile of modulation amplitude and phase. Symbols indicate corresponding chord position of the interferometer. Dotted lines are upper and lower error bar.

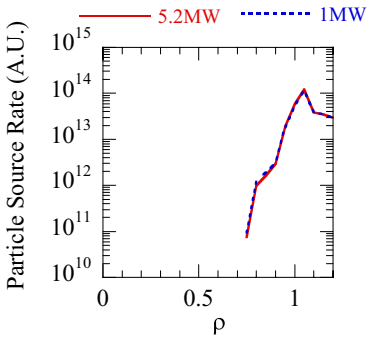

Figure 8. Profile of particle source rate from DEGAS code.

have good sensitivity because of the integration effects. After several trials of the model, it was decided that the model with four fitting parameters should be used.

The profiles of D and V are each described by two parameters. One is the core value (D_{core}, V_{core}), and the other is the edge value (D_{edge}, V_{edge}). The profiles of D are assumed to be flat in the core and edge and change at $\rho = 0.7$. The value of V is zero at $\rho = 0$, and V profiles are assumed to vary linearly with ρ, changing slope at $\rho = 0.7$. The values of V at $\rho = 0.7$ and $\rho = 1.0$ are taken to represent V_{core} and V_{edge}, respectively. The transition points of D and V are fixed at $\rho = 0.7$, because density gradients change at around $\rho = 0.7$ as shown in figures 1 and 5 suggesting that transport changes at this location.

Two fitting metrics χ^2_{total} and $\chi^2_{\mathrm{mod\_int}}$ were tried in order to study the non-linear effect. The best fitted D and V are shown in figure 9 for both cases. The error analysis was done similarly to the reconstruction of modulation components. Then the standard deviation of the best fitted D and V of each fitting calculation is defined as a fitting error. A quasi-Newton method was used for the fitting.

As shown in figure 9, the best fitted D of χ^2_{total} fitting and $\chi^2_{\mathrm{mod\_int}}$ fitting differs by about factor 1.5 in both heating cases, and the best fitted V almost agrees within the error bar, although the $\chi^2_{\mathrm{mod\_in}}$ fitting error bar of V in the 5.2 MW case is slightly large. Figure 10 shows a comparison of the line integrated amplitude and phase profile. The fitting procedure was done to minimize the difference between the experimental observed and calculated integrated profile. Figure 11 shows the comparison of the radial amplitude and phase profile between reconstructed profiles and calculated profiles using best fitted

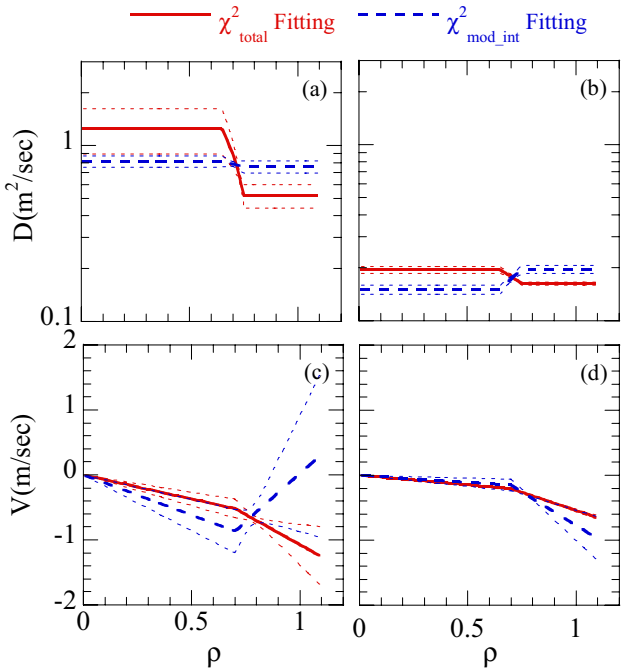

Figure 9. Comparison of $\chi^2_{\rm total}$ and $\chi^2_{\rm mod\_int}$ fitting. Diffusion coefficients profile of (*a*) 5.2 MW and (*b*) 1 MW heating. Convection velocity profiles of (*c*) 5.2 MW and (*d*) 1 MW heating. The dotted lines indicate upper and lower errors of the fitting.

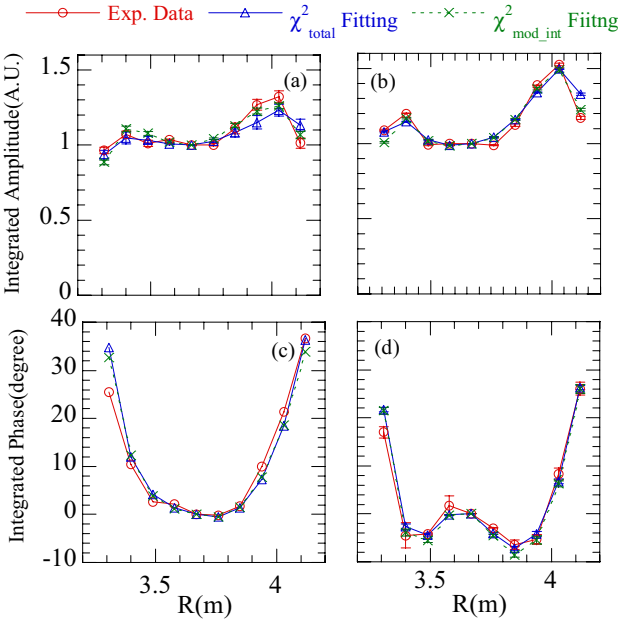

Figure 10. Comparison of $\chi^2_{\rm total}$ and $\chi^2_{\rm mod\_int}$ fitting of integrated amplitude (*a*),(*b*) and phase profile(*c*),(*d*). (*a*),(*c*) are 5.2 MW heating case and (*b*),(*d*) are 1 MW heating case.

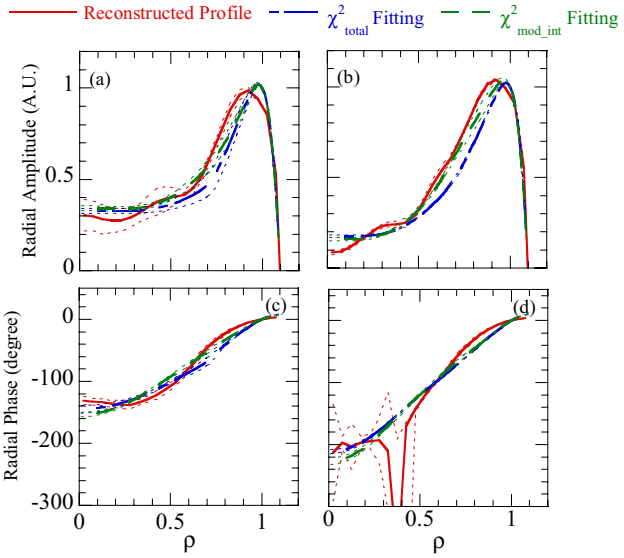

Figure 11. Radial amplitude (*a*),(*b*) and phase profile (*c*),(*d*) using $\chi^2_{\rm total}$ and $\chi^2_{\rm mod\_int}$ fitting result. (*a*),(*c*) are 5.2 MW heating case and (*b*),(*d*) are 1 MW heating case.

D and V. As shown in figures 10 and 11, experimental observation and calculated profiles are well agreed; however, there is a non-negligible difference. For better fitting, it may be necessary to increase the number of fitting parameters. However, for stable fitting additional experimental information will be required. The recently developed CO_2 infrared laser imaging interferometer [3] and microwave pulse radar reflectometry are expected to contribute to better fitting [17].

Figure 12 shows the comparison of the equilibrium profile from reconstruction and the calculated profile for two fitting schemes. As shown in figure 12(*b*), the reconstructed profile, $\chi^2_{\rm total}$ fitting profile and $\chi^2_{\rm mod\_int}$ fitting profile agree within the error bar in the 1 MW heating case. However, a not-significant but non-negligible difference between the reconstructed and $\chi^2_{\rm mod\_int}$ fitting profile is observed in the 5.2 MW heating case. This suggests that there may be a modest non-linearity at 5.2 MW heating case. For a more detailed study of the non-linearity, a scan of the modulation amplitude under the same condition will be necessary [18]. In particular, the effects of the temperature, temperature gradient and their perturbation effects should be considered in a future study. The observation of density modulation due to temperature modulation by heating modulation will help to clarify these issues.

4. Characteristics of transport coefficients

In this section parameter dependences of D and V are described. A systematic scan of the NBI heating power (P = 1–8.5 MW) was carried out at $R_{\rm ax}$ = 3.6 m. The data sets are obtained from the LHD 5th (2001–2002), 7th (2003–2004) and 8th (2004–2005) experimental campaigns. Totally 52 shots are used for the parameter dependence study. Eighteen shots were taken at 1.49 T in the 7th campaign, 5 shots at 2 T in the 8th campaign, 19 shots at 2.75 T in the 7th campaign and 10 shots at 2.8 T in the 5th campaign. Figure 13 shows the distribution of the temperature and density. During the scan of the heating power and $B_{\rm t}$, it was intended to keep the density constant; however, because of the lack of full controllability of density, there was a distribution of the equilibrium density.

The modulation frequency was 2 and 5 Hz for the 5th campaign, 10 Hz for the 7th campaign and 5 Hz for the 8th campaign data. Four fitting variables, $D_{\rm core}$, $D_{\rm edge}$, $V_{\rm core}$ and $V_{\rm edge}$, were used for the analysis of 2 and 5 Hz modulation.

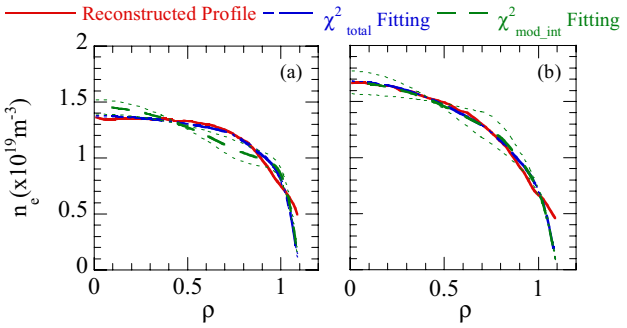

Figure 12. Radial equilibrium profile using $\chi^2_{\rm total}$ and $\chi^2_{\rm mod\_int}$ fitting result. (*a*) 5.2 MW heating case and (*b*) 1 MW heating case.

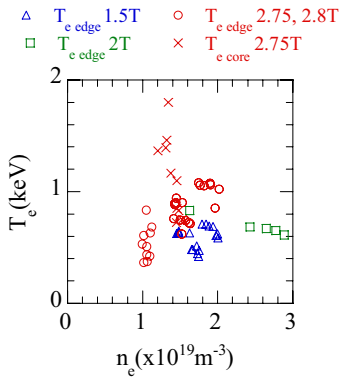

Figure 13. The distribution of the density and temperature of the dataset. The core and edge values are the averaged values between $\rho = 0.4$ and 0.7, and between $\rho = 0.7$ and 1.0, respectively.

Three fitting variables, spatially constant D, $V_{\rm core}$ and $V_{\rm edge}$, were used for the analysis of 10 Hz modulation.

Investigated plasmas lie in the plateau and the so-called $1/\nu$ regime, where the helical ripple transport is enhanced. The normalized collisionality ($\nu^*_{\rm h}$) was in the range of 0.26–2.6 at $\rho = 0.75$ for these shots. The normalized collisionality was defined as $\nu^*_{\rm h} = \nu_{\rm ei} q {\rm R}/\varepsilon^{1.5}_{\rm h,eff} {\rm v}_{\rm th\_e}$, where $\nu_{\rm ei}$ is the electron–ion collision frequency, q is the safety factor, R is the major radius, $\varepsilon_{\rm h,eff}$ is the effective helical ripple, and $\rm v_{th\_e}$ is the thermal velocity of the electron. The boundary of the plateau and $1/\nu$ regime corresponds to $\nu^*_{\rm h} = 1$. The gas species is hydrogen.

4.1. Comparison with neoclassical values and thermal diffusivities

The comparison of experimentally estimated transport coefficients with neoclassical transport coefficients is important to understand fundamental characteristics of transport. The neoclassical transport of the helical and stellarator device is larger than that in tokamaks because of the existence of magnetic ripples. If the transport is dominated by neoclassical transport, the optimization of the magnetic configuration should be focused to minimize neoclassical transport with good MHD instabilities. In this case, the turbulence study will not be important anymore. Figure 14 shows comparison with neoclassical transport of D and V in two different heating cases. The neoclassical estimation was calculated by the DCOM code [19]. As shown in figure 14(*a*),

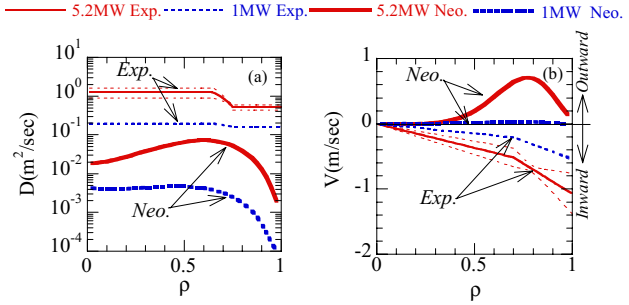

Figure 14. Experimental values and neoclassical estimation of (*a*) particle diffusion coefficients and (*b*) particle convection velocity.

the diffusion coefficients are about one order larger than the neoclassical estimation.

The comparison of the convection velocity was done as follows. The electron particle flux of the neoclassical theory can be written by the following equation [20].

$$\Gamma_{\rm e\_neo} = -nD_1 \left\{ \frac{\nabla n_{\rm e}}{n_{\rm e}} + \frac{eE_r}{T_{\rm e}} + \left(\frac{D_2}{D_1} - \frac{3}{2} \right) \frac{\nabla T_{\rm e}}{T_{\rm e}} \right\}. \quad (13)$$

Here, E_r is the radial electric field and e is charge of electron. Comparing with equation (1), the neoclassical convection velocity is defined as follows:

$$V_{\rm e\_neo} = -D_1 \left\{ \frac{eE_r}{T_{\rm e}} + \left(\frac{D_2}{D_1} - \frac{3}{2} \right) \frac{\nabla T_{\rm e}}{T_{\rm e}} \right\}. \quad (14)$$

Comparisons are shown in figure 14(*b*). In equation (14), the second term, which is $\nabla T_{\rm e}/T_{\rm e}$ term, dominates over the first term in these two cases of the experiments. Although the neoclassical theory predicts outward directed convection, experimental observation yields inward directed convection. The particle convection as well as particle diffusion is anomalous. Therefore, a turbulence study and consideration of the model of anomalous transport on LHD as well as on the tokamak is essential.

Figure 15 shows a comparison of the particle diffusion coefficients with thermal diffusion coefficients obtained from the power balance analysis by using the PROCTR [21] code. As shown in figure 15, both D and $\chi_{\rm e}$ are larger in the core in these cases. Typically, the $\chi_{\rm e}$ profiles have larger values in the core for the LHD standard configuration [22]. The value of $\chi_{\rm e}$ is larger than D. This is similar to the case of typical tokamak experiments.

4.2. Parameter dependence of the particle diffusion

The temperature dependence of D forms the basis for the investigation of the anomalous transport model. The simplest models for comparisons are Bohm-like and gyro-Bohm like diffusion. For Bohm-like diffusion, where particle transport is influenced by the long-wavelength fluctuations (up to plasma minor radius), D is proportional to $T_{\rm e}$, while for gyro-Bohm-like diffusion, where short-wavelength fluctuations (around the ion gyro-radius) play a role, D is proportional to $T_{\rm e}^{1.5}$ [23]. In tokamaks, the diffusion coefficients of dissipative and collisionless trapped electron mode is proportional to $T_{\rm e}^{3.5}$ [24] and $T_{\rm e}^{1.5}$, respectively [25]. The ion temperature

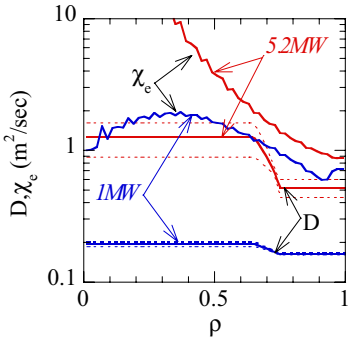

Figure 15. Comparison between particle diffusion coefficients and thermal diffusion coefficients.

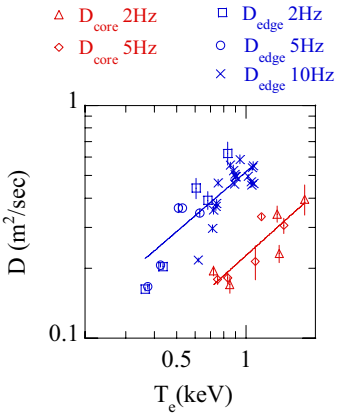

Figure 16. Electron temperature dependence of particle diffusion coefficients at $R_{ax} = 3.6$ m, $B_t = 2.75$, 2.8 T. $D_{edge} \propto T_e^{0.89\pm0.19}$ and $D_{core} \propto T_e^{0.85\pm0.13}$. The electron temperature is that averaged over the region $\rho = 0.4 \sim 0.7$ for the core, and $\rho = 0.7 \sim 1.0$ for the edge.

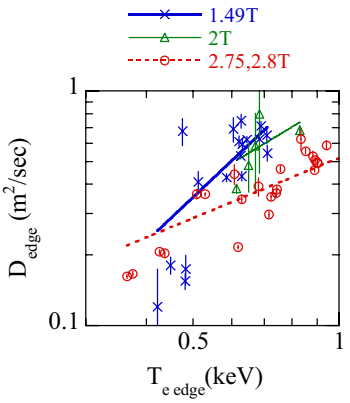

Figure 17. Electron temperature, which is averaged at $\rho = 0.4 \sim 0.7$, dependence of edge particle diffusion coefficients under different toroidal magnetic fields. $D_{edge} \propto T_e^{1.95\pm0.54}$ at 1.49 T, $D_{edge} \propto T_e^{1.25\pm1.02}$ at 2 T and $D_{edge} \propto T_e^{0.89\pm0.19}$ at 2.75, 2.8 T.

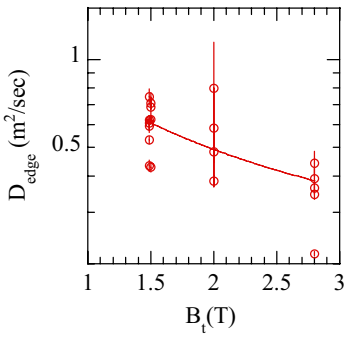

Figure 18. The toroidal magnetic field dependence of the edge particle diffusion coefficients under similar electron temperature (T_e edge (averaged at $\rho = 0.7 \sim 1.0$) $= 0.6 \sim 0.7$ keV). $D_{edge} \propto B_t^{-0.73\pm0.23}$.

gradient mode in the dissipative trapped electron regime of collisionality scales as $T_e^{3.5}$ [26]. In this section, an overview of the temperature and toroidal magnetic field dependence is reported. A detailed comparison with the theoretical model of turbulence is planned for the future.

Figure 16 shows the T_e dependence of D. The data set contains discharges at $B_t = 2.8$ and 2.75 T. The electron temperature is that averaged over the region $\rho = 0.4$–0.7 for the core, and $\rho = 0.7$–1.0 for the edge. The small difference of B_t is not expected to affect the transport. As shown in figure 16, no clear discrepancy of the estimated D is seen between different modulation frequencies. In both edge and core regions, positive temperature dependences were observed, which is typical for turbulence dominate transport. The diffusion coefficients vary with T_e as $D_{edge} \propto T_e^{0.89\pm0.19}$ and $D_{core} \propto T_e^{0.85\pm0.13}$. No clear difference between T_e dependence of D_{core} and that of D_{edge} was found.

Figure 17 shows D_{edge} versus T_e plots under different B_t. The observed T_e dependences are $D_{edge} \propto T_e^{1.95\pm0.54}$ at 1.49 T, $D_{edge} \propto T_e^{1.25\pm1.02}$ at 2 T and $D_{edge} \propto T_e^{0.89\pm0.19}$ at 2.75, 2.8 T. Although, at 2 T, the amount of data is limited (5 shots) and the dynamic range of T_e scanning is small, an increase of the temperature index as B_t decreases is pronounced. This suggests that the turbulence character changes under different B_t. Figure 18 shows the variation of D_{edge} with B_t. Here, the data, whose edge T_e varies from 0.6 keV to 0.7 keV are shown. Ten shots at 1.49 T, 4 shots at 2 T and 5 shots at 2.75, 2.8 T are used for the analysis. Then, the found B_t dependence is $D_{edge} \propto B_t^{-0.73\pm0.23}$.

As described above the observed variations of T_e and B_t from the present dataset do not correspond to simple Bohm-like ($\propto T_e/B_t$) or gyro-Bohm like ($\propto T_e^{1.5}/B_t^2$) law. Further consideration comparing the possible theoretical model is necessary to explain the observed dependences.

4.3. Parameter variation of the particle convection

In the core region, the existence of convection is obvious. The particle source is negligible at $\rho < 0.7$. So, in this region, the equilibrium particle flux should be zero under the equilibrium state ($\partial n_e/\partial t = 0$, $S = 0$ in equation (2)). Then, if density gradients exist in this area, diffusive and convective flux should be balanced. For example, in the peaked density profile the outward directed diffusive flux is balanced with the inward directed convective flux. In the hollow density profile, the inward directed diffusive flux is balanced with the outward directed convective flux.

In the edge region, the existence of the non-zero convection is not obvious from the equilibrium profile. However, the present analysis shows that having a non-zero convection gives better fits for both equilibrium and

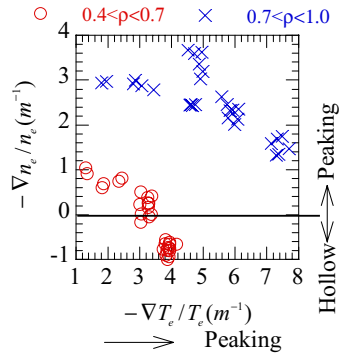

Figure 19. The relation between normalized temperature and density gradient. The core and edge values are estimated from the averaged value in core ($0.4 < \rho < 0.7$) and edge ($0.7 < \rho < 1.0$) at $R_{ax} = 3.6$ m, $B_t = 2.75$, 2.8 T. The 29 shots from figure 16 are shown.

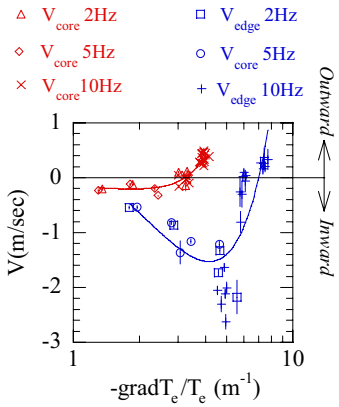

Figure 20. The dependence of the convection velocity on the normalized electron temperature gradient. The normalized electron temperature gradient is that averaged over the region $\rho = 0.4 \sim 0.7$ for the core, and $\rho = 0.7 \sim 1.0$ for the edge.

modulation profiles. Once V becomes non-zero in the core, because of the continuity of the D and V profile, the existence of V may be required in the edge region as well. However, we cannot deny completely the possibility that the equilibrium and modulation profiles can be described only by D, which has spatial distribution, in the cases where V is negligible in the core, and V is non-zero in the edge.

Hollow density profiles are observed in LHD in many discharges. This is in harsh contrast to tokamak plasmas, where most density profiles are peaked.

Figure 19 shows the relation of normalized temperature and density gradients estimated in the core and edge regions at $R_{ax} = 3.6$ m and $B_t = 2.75$, 2.8 T. There is a strong linkage between the density and temperature gradients both in core and edge regions. This suggests that convective flux is driven by the T_e gradient. Therefore, the dependence of the convection velocities on the normalized T_e gradient ($\nabla T_e/T_e$) was studied.

Figure 20 shows the plot of V versus the normalized T_e gradient. The values of V at $\rho = 0.7$ and at $\rho = 1.0$ are used to represent V_{core}, and V_{edge}, respectively. The electron temperature gradient is that averaged over the region $\rho = 0.4$–0.7 for the core, and $\rho = 0.7$–1.0 for the edge. As shown in figure 20, the modulation frequency does not affect dependence $V(\nabla T_e/T_e)$ as well as the dependence of $D(T_e)$.

In the core region, V_{core} is directed inward at lower $\nabla T_e/T_e$ and reverses the sign at higher $\nabla T_e/T_e$. On the other hand, in the edge region, $\nabla T_e/T_e$ dependence is more complicated. There is a minimum value of V_{edge}. As the normalized temperature gradient increases, V_{edge} decreases to the inward direction and reaches inward peak, then finally reverses direction from inward to outward.

The variation of the toroidal magnetic field produces additional effects. Figure 21 shows T_e and n_e profiles under different B_t. As shown in figure 21, temperature profiles are almost identical; however, very clear difference of the n_e profiles were observed. Figure 21 suggests strong outward convection in the core at 1.49 T and smaller convection at 2.75 T under the same T_e gradient. The toroidal magnetic field is an additional parameter to determine the convection.

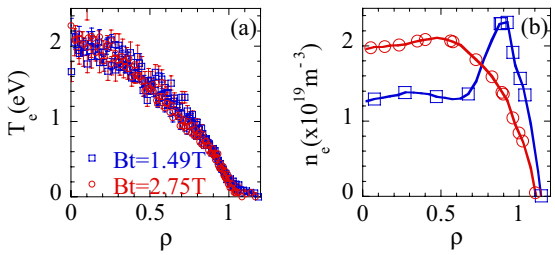

Figure 21. Comparison of (*a*) electron temperature and (*b*) density profiles under different toroidal magnetic fields. Symbols in figure 21(*b*) indicate corresponding FIR and CO_2 laser interferometer chord position.

Figure 22 shows $\nabla T_e/T_e$ dependence of V_{core} and V_{edge} under different magnetic fields. As shown in figure 22, both V_{core} and V_{edge} tend to be larger and more outward directed at the same $\nabla T_e/T_e$ as B_t decreases.

5. Characteristics of turbulence

As described in section 4.1, transport is dominated by the anomalous one. To get a comprehensive picture of particle transport, it is necessary to measure microturbulence. The spectrum and the spatial structure of fluctuations, dependence on the parameters of the discharge and correlation with transport characteristics can provide ideas to understand anomalous transport. In LHD, microturbulence was measured using a CO_2 laser phase contrast imaging (PCI) interferometer [27–29]. Preliminary measurements of the radial wave number components in the edge region show enhanced fluctuation amplitude and reduction of peak wave number when energy confinements degrade at lower magnetic field [27]. In this section, the results obtained using the recently developed two-dimensional (2-D) phase contrast interferometer [28, 29] are reported. Since the length of the scattering volume for the expected wavenumber region is larger than the plasma size for the 10.6 μm infrared CO_2 laser wavelength, no spatial resolution is expected along the beam axis by using the conventional scattering technique. However,

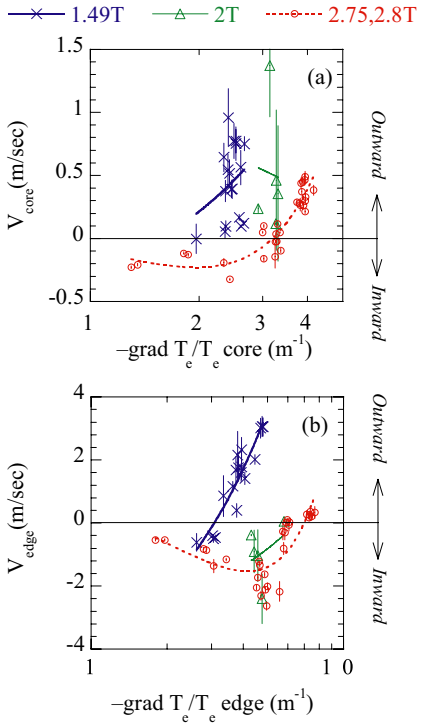

Figure 22. The dependence of the convection velocity on normalized electron temperature gradient under different magnetic fields. (*a*) Core and (*b*) edge convection. The normalized electron temperature gradient is that averaged over the region $\rho = 0.4 \sim 0.7$ for the core, $\rho = 0.7 \sim 1.0$ for the edge.

by using the strong magnetic shear of LHD, it is possible to get modest spatial resolution along the probe beam [28–30].

5.1. Spatial structure of turbulence

By using a 48 (6 by 8) channel 2-D detector, it is possible to get the fluctuation profile from a single shot at a particular time by taking advantage of the strong magnetic shear. The two-dimensional PCI (2D PCI) records the 2-D fluctuation picture integrated along the injected beam direction. This 2-D picture contains images of fluctuations propagating perpendicular to magnetic field lines, along the path of the probe beam. The propagation direction can be resolved by the spatial 2-D Fourier transform. The location of the fluctuation can be determined from the position of the field, which is perpendicular to the propagation direction [28, 29].

Figure 23 shows a poloidal cross-section of the measurements. The view area at $R = 3.825$ m is 6.1 (major radial direction) × 17.5 mm (toroidal direction). The sampling space is 1.05 mm separation along the major radius with 6 channels and 2.38 mm along the toroidal direction with 8 channels. The accessible regions are $|\rho| \geqslant 0.4$, which are determined by the position of the chord as shown in figure 23. Frequencies can be measured within the range of $f = 5$–500 kHz and wavenumbers within $k = 0.3$–1.5 mm^{-1}. The wave vectors are projections to the perpendicular direction of the beam axis as indicated by the thick arrows in figure 23. Thus the observed fluctuations are dominated by the poloidal components in the present configuration.

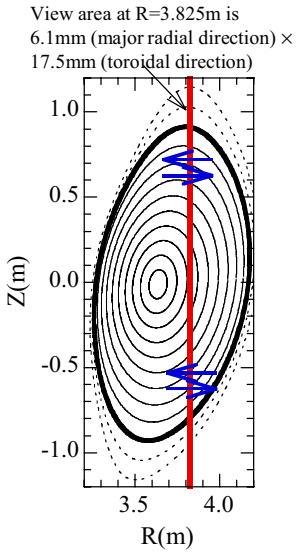

Figure 23. Measured cross section of phase contrast interferometer. Magnetic flux surfaces are shown every $\rho = 0.1$ step from $\rho = 0.1$ to 1.2. Magnetic configuration is standard configuration ($R_{ax} = 3.6$ m). The thick vertical line marks the path of CO_2 laser beam.

Figure 24(*a*) shows T_e and n_e profiles of the target of the measurements, and figure 24(*b*) shows an example of the spatial structure of the microturbulence. The magnetic configuration is the standard configuration ($R_{ax} = 3.6$ m), and B_t is 2.75 T. A peaked T_e and hollow n_e profiles are observed as shown in figure 24(*a*). The density modulation was done for the investigation of the particle transports. The estimated values of D_{core} and D_{edge} are 0.09 ± 0.002, 0.08 ± 0.003 m^2 s^{-1} and V_{core} and V_{edge} are 0.047 ± 0.095 (outward directed), -0.245 ± 0.075 (inward directed) m s^{-1}. The values of D and V differ from the expected values of figures 16 and 20, because the density in figure 24 is a factor 2–3 higher than that of the data sets described in section 4. Here, the higher density shot was selected to measure the detailed structure of the fluctuation profiles with good signal intensity. The maximum entropy method (MEM) was applied to get fine spectral resolution. The many structures can be clearly seen in figure 24.

Since fluctuations along the beam axis in figure 23 contribute to the signal, fluctuations from the upper and lower of equatorial plane can be distinguished. The spectrum in the positive and negative ρ regions corresponds to the top and bottom part of the measured cross section in figure 23. The poloidally rotating fluctuations have opposite directions in the top and bottom as shown by the thick arrow in figure 23; therefore, such fluctuation components have opposite signs in the top and bottom regions in figure 24.

The spatial resolution is around $\Delta\rho = 0.1$–0.2. Asymmetries between the top and bottom region are observed; however, the structures are similar in both regions. In figure 24, the $E_r \times B_t$ poloidal rotation velocity is marked with a blue line, and the velocity remainder after the subtraction of the drift velocity from $E_r \times B_t$ poloidal rotation velocity is shown by the green line. These are the references of the phase velocity of fluctuation in the plasma frame.

The radial electric field is calculated from the ambipolar condition of neoclassical theory by the GSRAKE code [31]

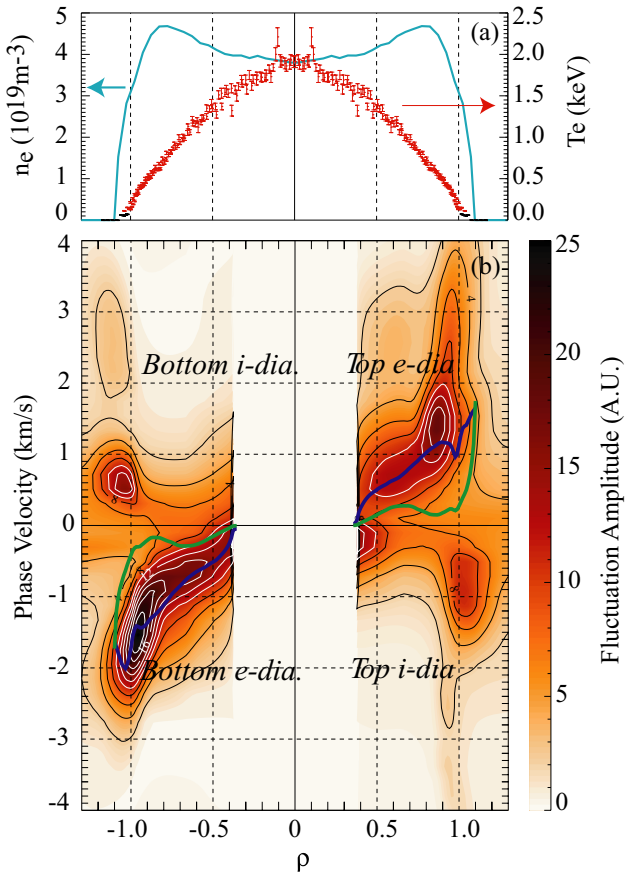

Figure 24. (*a*) T_e and n_e profiles of target of the fluctuation measurements and (*b*) contour plot of fluctuation amplitude measured by 2D PCI. Dark colour indicates stronger intensity. The dimension of the amplitude is arbitrary units. Positive and negative ρ indicate the bottom and top part of measured position along beam axis in figure 23, respectively. Positive velocity in the top part and negative velocity in the bottom part indicate electron diamagnetic direction in the laboratory frame. Negative velocity in the top part and positive velocity in the bottom part indicate ion diamagnetic direction in the laboratory frame. Blue lines mark $E_r \times B_t$ poloidal rotation velocity and green lines show the remainder after substraction ($\nabla P \times B_t$)-diamagnetic drift velocity from $E_r \times B_t$ velocity.

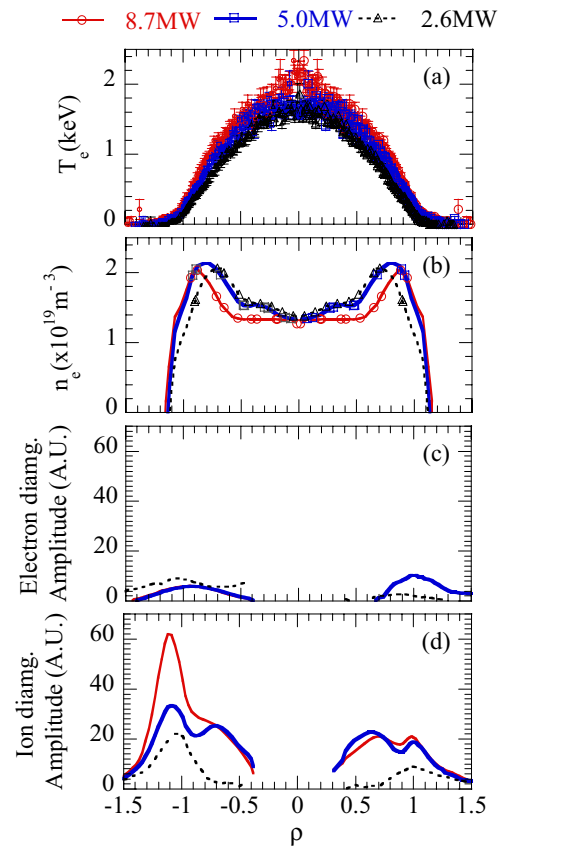

Figure 25. Comparison of the profile at 1.49 T under different NBI heating power (*a*) T_e profile, (*b*) n_e profile (*c*) electron diamagnetic and (*d*) ion diamagnetic direction propagating fluctuation amplitude profile.

with the measured T_e and n_e profiles of figure 24(*a*). The calculated E_r from the neoclassical ambipolar condition agrees reasonably with measured E_r by charge exchange spectroscopy [32], which is not available in the discharge of figure 24. The diamagnetic drift velocity was calculated by the following equation with the measured T_e and n_e profile in figure 24(*a*).

$$V_{\mathrm{diag\_drift}} = \frac{\nabla P}{e n_e B_t} = \frac{k_B T_e}{e B_t}\left(\frac{1}{n_e}\frac{\mathrm{d}n_e}{\mathrm{d}r} + \frac{1}{T_e}\frac{\mathrm{d}T_e}{\mathrm{d}r}\right), \qquad (15)$$

where k_B is the Boltzmann constant.

The fluctuation has a peak at $\rho = \pm 0.9$, and the fluctuation also exists in the positive density gradients region, where $|\rho| < 0.8$. In the positive density gradients region, phase velocities are close to the $E_r \times B_t$ poloidal rotation. In the negative density gradient region, where $|\rho| > 0.8$, the phase velocity increases in the electron diamagnetic direction in the laboratory frame and then switches direction to the ion diamagnetic direction at around $|\rho| = 1.0$. This switch indicates that a strong velocity shear is formed at this location. The accuracy of the profile of the $E_r \times B_t$ and drift velocity depends on the accuracy of the profile measurements. In addition, careful comparison needs good accuracy in determination of the phase velocity profile of fluctuation. Presently, detailed comparison is difficult, and measurements of E_r and improvement in the spatial resolution of the fluctuation measurements are required. However, it is possible to say that fluctuations propagate in the ion diamagnetic direction in the plasma frame at $|\rho| \geqslant 1.0$, where n_e and T_e are not zero yet. The ion temperature gradients mode may be one candidate to explain these edge fluctuations.

5.2. *Fluctuation and particle transport*

In this section, the linkage between the observed fluctuation and particle transport is examined. Figure 25 shows n_e, T_e and fluctuation amplitude ($\tilde{n}_e$) under different heating power at $B_t = 1.49$ T. These are from the data set described in section 4. As shown in figure 25(*b*), hollow density profiles are observed in all three cases, and the peak density position shifts to outward as heating power increases. This is because V_{edge} increases in the outward direction at a higher temperature gradient as described in section 4.3.

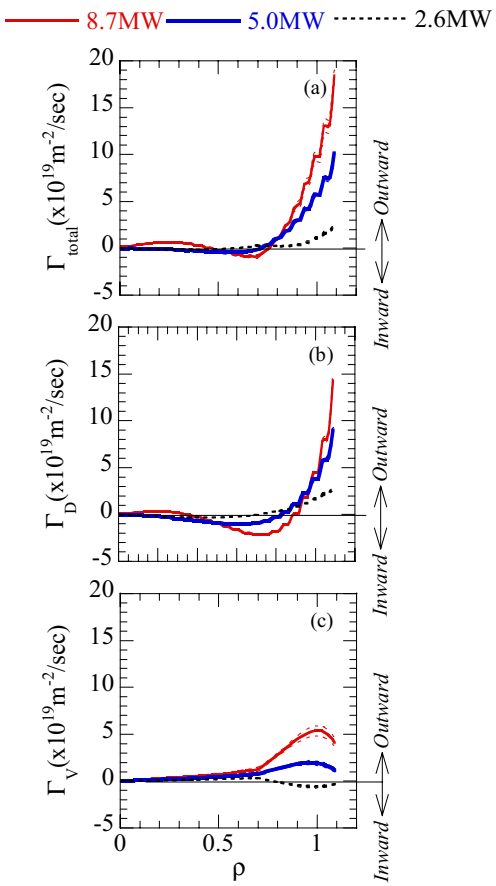

Figure 26. Profiles of (*a*) total (*b*) diffusive and (*c*) convective particle flux. D is 0.18, 0.43 and 0.71 $m^2\,s^{-1}$ at 2.6, 5.0 and 8.7 MW, respectively. V_{core} is 0.17,0.39 and 0.75 $m\,s^{-1}$ at 2.6, 5.0 and 8.7 MW, respectively. V_{edge} is −0.49, 1.17 and 3.07 $m\,s^{-1}$ at 2.6, 5.0 and 8.7 MW, respectively. Dashed lines show the fitting error of D and V.

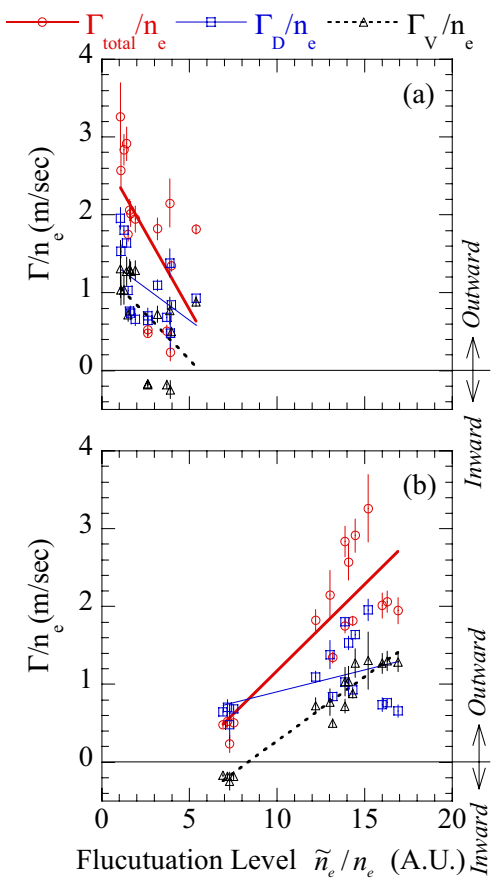

Figure 27. Relation of fluctuation level $\tilde{n}_e/n_e$ and normalized particle flux at $B_t = 1.49$ T. (*a*) Electron diamagnetic and (*b*) ion diamagnetic direction propagating fluctuation level. The error of the normalized flux is due to the fitting error of D and V.

Both ion and electron diamagnetic propagating fluctuations in the laboratory frame as shown in figure 24 are generally observed in the present dataset. However, it is difficult to determine the spatial location of low k components. Figures 25(*c*) and (*d*) show the fluctuation profile of fluctuations propagating in the electron and ion diamagnetic directions. Wavenumbers of these fluctuations are larger than 0.5 $m\,m^{-1}$, so location determination is possible. The radial electric field is estimated to be around zero by the GSRAKE code from the neoclassical ambipolar condition in the present dataset. Recent results of the E_r measurements show good agreement with the neoclassical prediction, where the averaged density is around 1.5×10^{19} m^{-3}, and the central temperature is 1.5–2 keV at $R_{ax} = 3.6$ m [33]. Therefore, electron and ion diamagnetic propagation in the laboratory frame are the same as in the plasma frame. The fluctuation amplitude becomes larger with higher heating power.

Figure 26 shows the profile of the particle flux of three cases. These are calculated using the estimated D, V from the modulation experiments and measured n_e profiles. The density profiles were fitted with a polynomial function to make the gradient smooth. The total flux is described by equation (1), and diffusive and convective fluxes are described by the first and second terms of equation (1).

Figure 27 shows the relationship between the fluctuation level ($\tilde{n}_e/n_e$) and the normalized particle flux. The fluctuation level was calculated separately for electron and ion diamagnetic direction propagating components. Figure 27 consists of 16 shots. Here, the fluctuation level is the ratio of the observed fluctuation amplitude, which is averaged between $|\rho| = 0.7$ and $|\rho| = 1.1$ and $k > 0.5\,mm^{-1}$ and $5 < f < 500$ kHz, to the averaged density at $0.7 < \rho < 1.1$. Because the spatial resolution of the fluctuation measurements are not very fine, average fluctuation levels are used. The normalized particle flux is calculated also at $0.7 < \rho < 1.1$.

A clear positive correlation is seen between the normalized particle flux and ion diamagnetic direction propagating fluctuation level. At the higher ion diamagnetic direction propagating fluctuation level, normalized particle flux becomes higher. However, a clear relation is not seen between the electron diamagnetic direction propagating fluctuation level and the normalized particle flux. This suggests that the observed ion diamagnetic direction propagating fluctuation plays a role in edge particle transports. Present results show that the ion diamagnetic direction propagating fluctuation shows positive correlation with both diffusive and convective flux.

For the quantitative analysis, not only the density fluctuation but also potential fluctuation amplitude and the

phase relation between density and potential fluctuation are required. Although potential fluctuations are difficult to measure experimentally in the present regime, with the help of theoretical models, more detailed consideration will be possible. This is a future subject of study.

6. Summary and discussion

Density modulation experiments have been carried out on both the tokamak and stellarator. Reported parameter dependences of D and V vary on different devices. With regard to the T_e dependence of D, a modest dependence ($\propto T_e$) was reported in JET [34], and stronger dependence ($\propto T_e^2$) was reported in TFTR [14]. In W-7AS, the diffusion coefficient was found to be proportional to $n_e^{-1.18\pm0.13}$, $T_e^{0.69\pm0.22}$ and $B_t^{-0.51\pm0.22}$ [35]. In addition to the variety of the results inter devices, the temperature dependence is different in LHD at various magnetic fields. These results indicate that anomalous diffusion is very complicated. A systematic scan of n_e, T_e, B_t at each device will provide a more general view. The comparison under the same dimensionless parameters, which are ν^*, ρ^* and β, may be another possible approach.

Recently, interest has been aroused in the inward directed particle pinch in tokamaks [36,37]. These inward pinches have been observed with a negligible parallel electric field indicating that they are not due to the ware pinch. They may be interpreted as being driven by $\nabla q/q$ and $\nabla T_e/T_e$. The pinch driven by $\nabla q/q$ is called curvature pinch and that deriven by $\nabla T_e/T_e$ is called thermo-diffusion. The observed density peaking was interpreted as being a result of the curvature pinch with a dominant trapped electron mode [38, 39]. Then, the control of density peaking can be done by a q profile control. On the other hand, the q profile does not influence the density profile in LHD. For example, in figure 1, all shots have low beta (<0.3%), so the q profiles are almost identical. However, a dramatic change of density profiles, resulting primarily from a change in V, is observed. The control of the temperature profile is more effective in changing the density profile in LHD. A similar behaviour was reported in W-7AS, whose $\nabla q/q$ are very flat. Density profiles were changed from peaked to flat by modifying the T_e profile according to the ECRH resonance position [40]. These differences in the character of the particle pinch between tokamak and helical/stellarator devices might be due to the difference in magnetic ripple.

Understanding of turbulent driven transport is an essential issue both in tokamak and helical/stellarator devices. However, not many measurements have been made to make a quantitative linkage with transport. Not only density fluctuations but also potential, temperature and magnetic field fluctuations and their correlations are necessary to understand the complete picture of turbulent driven transport. However, even with the present diagnostic and experimental technique, the systematic comparison between observed density fluctuations and particle transport, described in this paper, can provide insight into the nature of anomalous transport. A more detailed systematic study of particle transport and fluctuation characteristics, including the density dependence, effect of magnetic configuration and comparison with theoretical anomalous transport models [41], is planned.

References

[1] Narihara K. *et al* 2001 *Rev. Sci. Instrum.* **72** 1122
[2] Kawahata K. *et al* 1999 *Rev. Sci. Instrum.* **70** 707
[3] Tanaka K. *et al* 2004 *Rev. Sci. Instrum.* **75** 3429
[4] Yamada H. *et al* 2001 *Nucl. Fusion* **41** 901
[5] Goto M. *et al* 2002 *Contrib. Plasma Phys.* **42** 616
[6] Tanaka K. *et al* 2001 *J. Plasma Fusion Res. Ser.* **4** 427
[7] Gentle K.W. *et al* 1987 *Plasma Phys. Control. Fusion* **29** 1077
[8] Heifetz D. *et al* 1982 *J. Comput. Phys.* **46** 309
[9] Shoji M. *et al* 2005 *J. Nucl. Mater.* **337–339** 186
[10] Nagashima K. and Sakasai A. 1992 Rep. JAERI-M 92-057.JAERI, Ibaraki
[11] Tanaka K. *et al* 2005 *J. Plasma Sci. Technol.* at press
[12] Lopes Cardozo N.J. 1995 *Plasma Phys. Control. Fusion* **37** 799
[13] Inagaki S. *et al* 2006 *Nucl. Fusion* at press
[14] Efthimion P.C. *et al* 1991 *Phys. Rev. Lett.* **66** 421
[15] Tanaka K. *et al* 1999 *Proc. 26th European Physical Society Conf. on Controlled Fusion and Plasma Physics (Maastricht France, 14–18 June)* 1329
[16] Hirshman S.P. 1983 *Phys. Fluids* **26** 3553
[17] Kaneba T. *et al* 2004 *Rev. Sci. Instrum.* **75** 3846
[18] Gentle K.W. *et al* 1992 *Phys. Rev. Lett.* **68** 2444
[19] Murakami S. *et al* 2002 *Nucl. Fusion* **42** L19–22
[20] Trobaldos V. 2001 *Phys. Plasma* **8** 1229
[21] Howe H.C. 1993 *Proctr nid user and numerical guide* Oak Ridge, Tennesee 37831 Oak ridge national laboratory
[22] Yamada H. *et al* 2002 *Plasma Phys. Control. Fusion* **44** A245
[23] Kadomtsev B.B. 1992 *Tokamak Plasma: a Complex Physical System* (Beograd: IOP)
[24] Kadomtsev B.B. and Poguste B.P. 1970 *Rev. Plasma Phys.* **5** 249
[25] Adam J.C. *et al* 1976 *Phys. Fluids* **19** 561
[26] Terry P.W. *et al* 1989 *Phys Fluids* **B1** 109
[27] Tanaka K. *et al* 2003 *Rev. Sci. Instrum.* **74** 1633
[28] Sanin A. *et al* 2004 *Rev. Sci. Instrum.* **75** 3439
[29] Vyacheslavov L.N. *et al* 2005 *IEEE Trans. Plasma Sci.* **33** 464
[30] Kado S. *et al* 1995 *Japan. J. Appl. Phys.* **34** part 1, 6492
[31] Beidler C.D. *et al* 1994 *Plasma Phys. Control. Fusion* **36** 317
[32] Ida K. *et al* 2001 *Phys. Rev. Lett.* **86** 5297
[33] Ida K. *et al* 2005 *Nucl. Fusion* **45** 391
[34] O'Rourke J. *et al* 1993 *Plasma Phys. Control. Fusion* **35** 585
[35] Koponen J.P.T. *et al* 2000 *Nucl. Fusion* **40** 365
[36] Hoang G.T. *et al* 2003 *Phys. Rev. Lett.* **90** 155002-1
[37] Zabolotsky A. *et al* 2003 *Plasma Phys. Control. Fusion* **45** 735
[38] Garbet X. *et al* 2003 *Phys. Rev. Lett.* **91** 035001-1
[39] Hoang G.T. *et al* 2004 *Phys. Rev. Lett.* **93** 135003-1
[40] Stroth U. *et al* 1999 *Phys. Rev. Lett.* **82** 928
[41] Rewoldt G. *et al* 2002 *Nucl. Fusion* **42** 1047